Electronic Supplementary Material (ESI) for Energy & Environmental Science.

Electronic Supplementary Information

Thermally regenerative copper nanoslurry flow battery for heat-to-power conversion with low-grade thermal energy

Sunny Maye[a], Hubert H. Girault[a] and Pekka Peljo[a,b,*]

[a]Laboratoire d'Électrochimie Physique et Analytique, École Polytechnique Fédérale de Lausanne, EPFL Valais Wallis, Rue de l'Industrie 17, Case Postale 440, CH-1951 Sion, Switzerland

[b]Department of Chemistry and Materials Science, Aalto University, PO Box 16100, FI-00076 Aalto, Finland

*Corresponding Author:

Pekka Peljo, pekka.peljo@aalto.fi

Contents

Experimental details

Electrochemistry. Cyclic voltammetry (CV) and chronopotentiometry (CP) were performed inside a three electrode set-up with a Pt wire as counter electrode (CE) and a Pt disk working electrode (WE, dia. 2mm). The reference electrode (RE) was made with a Cu wire (dia. 1mm, ≥ 99.99%, GoodFellow) inside the solution containing 0.1 M $TEABF_4$ as a supporting electrolyte and 0.01 M $[Cu(CH_3CN)_4]BF_4$ in acetonitrile-propylene carbonate mixtures. Diffusion coefficients and rate constants were determined from CV at different temperatures.

Differential scanning calorimetry. Thermal analysis data were recorded by differential scanning calorimetry with a Mettler Toledo DSC 821e. Calculation and data treatment were handled with the STARe thermal analysis software from Mettler Toledo. When air sensitive compounds were targeted, samples were prepared under inert atmosphere inside a glove box. DSC crucibles avoid contamination of the DSC oven by the sample and have a pin for contact with the thermocouple wires (standard aluminum crucible with pin and 40 µL volume, model n° 00027331). As liquid samples are investigated, the lids of the pan need to be pierced for the evacuation of the gas after evaporation (aluminum lid pierced with 50 µm hole, model n° 51140832). Solid or liquid samples usually have a mass between 10 and 35 mg for a volume of 25 µL. The heat flow of the sample is determined versus an empty Al crucible reference with a heating rate (v) of 5, 10 or $20°C\cdot min^{-1}$. The DSC machine is composed of an outer chamber into which a flow of air is applied at 80 mL/min around the furnace to keep a constant environment and an inner chamber into which N_2 is introduced at 200 mL/min to protect the furnace from accumulation of oxygen and moisture, which may damage the cell. N_2 is also applied because it provides homogenous heat and heat transfer to the sample crucible. Before measurements (especially for heat capacity), the sample chamber is cleaned at a temperature of 500°C for 5 min with a stream of purging gas in order to remove dust and other contaminants (see below for an illustration of the DSC furnace). The DSC analysis is illustrated in detail in below.

Other analytical techniques. UV-vis spectroscopy was carried out with a ChemStation for UV-visible spectroscopy (Agilent Technologies, USA). Cu^{2+} samples from the thermal regeneration are filtered and centrifuged to remove the metallic Cu which is produced during the same reaction.

Raman spectra were measured at room temperature by an inVia Raman Microscope (Renishaw, UK) with a pulsed excitation line of 532 (Nd-YAG laser) or 633 nm (helium-neon laser). Liquid samples and the air sensitive $[Cu(CH_3CN)_4]BF_4$ powder were analysed inside a sealed UV-vis cuvette.

The images are recorded with a scanning electron microscope (SEM) and a transmission electron microscope (TEM). The SEM is a Teneo SEM (FEI, USA) equipped with a Schottky field emission gun. Secondary electron detection was achieved with an Everhart-Thornley detector and an in-lens detector. The TEM is a Tecnai G2 Spirit Twin (FEI, USA) equipped with a LaB_6 electron gun. For composition characterisation, X-rays are detected by energy-dispersive X-ray spectroscopy (EDX) (XFlash Silicon drift detector) inside the SEM.

Battery efficiency calculations

The Coulombic efficiency is defined as the ratio of the charge, which is given by the battery during the discharge ($Q_{\mathrm{discharge}}$), over the charge, which is accumulated during the previous charging process (Q_{charge}):

$$\eta_Q = \frac{Q_{discharge}}{Q_{charge}} \qquad (S1)$$

The energy efficiency is given by equation 2 as the ratio between the charge (I_{charge}) and discharge ($I_{\mathrm{discharge}}$) current. As the cell induced an Ohmic resistance, it is more useful to calculate the theoretical efficiency of a system with a minimal Ohmic drop. This allows a more accurate comparison of different systems. To be able to obtain this efficiency, the charge/discharge curves need to be corrected with Ohmic compensation. For that purpose, the resistance inside the cell is evaluated after each charging and discharging steps by chronopotentiometry. From these corrected potentials, the energy efficiency can be calculated with:

$$\eta_E = \frac{\left| I_{discharge} \int_{t_s}^{t_f} E\,dt \right|}{\left| I_{charge} \int_{t_0}^{t_s} E\,dt \right|} \qquad (S2)$$

DSC analysis

Typical DSC curves are plotted with the heat flow ($\dot{Q}$, defined in Equation 3) *versus* the temperature of the furnace. This $\dot{Q}$ represents the difference of heat, which is required for the sample to keep the same temperature as the reference:

$$\dot{Q} = \frac{dQ}{dt} = \dot{Q}_s - \dot{Q}_r \qquad (S3)$$

For a change of the sample physical state (melting/crystallization, evaporation, glass transition, decomposition (oxidation)), the heat flow curve is modified because more or less heat is provided to the sample for the state transition. From the integration of the exo or endothermic peak induced by the phase modification, the enthalpy of the process can be calculated if the mass (*m*) of the sample is known:

$$\Delta H = \int \frac{\dot{Q}}{m} dt \qquad (S4)$$

To determine the heat capacity of the sample, the so-called direct method is applied. The sequence starts with an isothermal step and is followed by a dynamic temperature period with a heating rate of 5°C·min^{-1}. The difference of heat flow between the two steps ($\Delta\dot{Q}_s$) depends on the C_p of the sample (Equation 5). With the C_p values of a mixture and the C_p^* value for the pure compounds, the excess heat capacity C_p^E can be calculated with Equation 6.

$$C_p = \frac{\dot{Q}}{m} * \frac{1}{dT/dt} = \frac{\Delta\dot{Q}_s - \Delta\dot{Q}_b}{m \cdot v} \qquad (S5)$$

$$C_p^E = C_p - (x_1 C_{p1}^* + x_2 C_{p2}^*) \qquad (S6)$$

Before each measurement, a blank curve has to be determined with an empty crucible to subtract the signal of the Al pan ($\Delta\dot{Q}_b$). The values for the enthalpies and heat capacity are calculated from the average of at least three different data curves.

Synthesis and characterization of Cu(I) salts

A well-known synthesis of Cu(I) complex is achieved in acetonitrile, which plays the role of solvent and ligand, during the comproportionation of Cu and Cu(II).[1–3] For this synthesis of $[Cu(CH_3CN)_4]BF_4$, copper(II) tetrafluoroborate hydrate ($Cu(BF_4)_2 \cdot xH_2O$, Sigma-Aldrich), acetonitrile (Merck) and copper wire (dia. 1 mm, $\geq$ 99.99%, GoodFellow) were of analytical grade and were used as received. The comproportionation reaction occurs in a Schlenk line with nitrogen. The Cu^+ complex with acetonitrile is dried overnight under vacuum and stored in a nitrogen-filled glove box. The reaction occurs with a constant heating around the boiling point of acetonitrile under inert atmosphere (N_2):

$$\mathrm{Cu} + \mathrm{Cu}^{2+} + 8\,\mathrm{CH_3CN} \xrightleftharpoons[\text{Under } \mathrm{N_2}]{\text{Reflux 83 °C}} 2\,\mathrm{Cu(CH_3CN)_4}^{+}$$

This reflux coupled to the Schlenk line is maintained until the blue solution containing Cu(II) changes to a totally transparent and uncolored phase. If the concentration of Cu(II) in the starting solution is high enough, some Cu(I) complexes can precipitate before removing the solvent. To separate the excess of copper, the solution is filtrated inside the glovebox to avoid contact of the sensitive Cu(I) with the oxygen and moisture coming from ambient air. During the last step, the Cu(I) complex is isolated by evaporating acetonitrile overnight under vacuum. The final aspect of the Cu(I) product is a white and shiny crystalline powder. According to the amount of metallic Cu, which reacts, and the quantity of produced Cu(I), the yield is calculated and reaches 97%. For a long-term storage, the Cu(I) powder is kept inside the glovebox.

As acetonitrile belongs to the C_{3v} group and contains 6 atoms, it can be calculated, according to the group theory, that this molecule has 12 vibrations modes. Among them, 8 modes coming from 4 doubly degenerated vibrations, arising from the E class, should appear at only 4 different wavelengths ν_5, ν_6, ν_7 and ν_8. The other 4 fundamental vibration modes ν_1, ν_2, ν_3 and ν_4 belong to the symmetric A_1 class.[4] All of them should be Raman and IR active.[5]

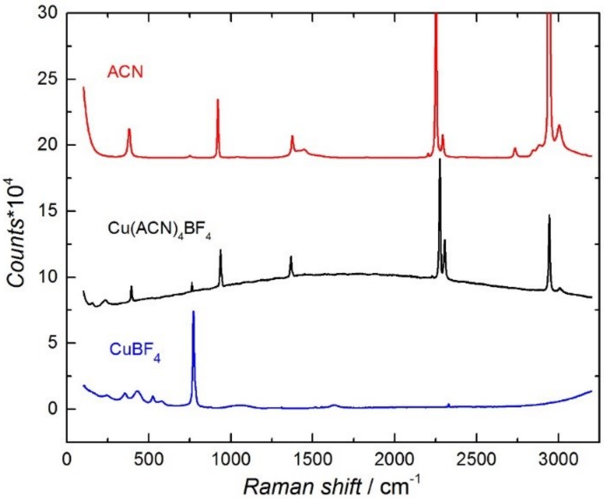

Supplementary Figure 1. Raman spectra of liquid acetonitrile (red), solid $[Cu(CH_3CN)_4]BF_4$ powder (black) and solid $Cu(BF_4)_2$ powder (blue).

In Figure S1, Raman spectra of liquid acetonitrile and solid $Cu(BF_4)_2$ are compared with acetonitrile, which is coordinated with Cu(I) as the solid $[Cu(CH3CN)_4]BF_4$ salt. Raman spectroscopy is obtained by the inelastic (anti-)Stokes scattering of an exciting light inside a molecules and gives it vibration levels.[4] A summary of the liquid acetonitrile vibrations and acetonitrile vibrations as a ligand is given in Table S1. The experimental Raman shifts of the different vibrational states are in good agreement with previous publications, which also help to attribute the mode, class and assignment of vibrations to the Raman shifts.[6–9] By analysing the similarities of the fingerprints between liquid CH_3CN and $[Cu(CH_3CN)_4]BF_4$, 9 peaks are in the same range of energy. Seven of them correspond to the fundamental modes vibrations and ν_7, which is of really low intensity in acetonitrile, doesn't appear in the Cu(I) complex. acetonitrile vibration energies vary from 0.1 to 5.4% between the two samples (Table S1). This effect was explained and predicted by Dimitrova with simulations of acetonitrile-cation interactions.[10] Vibrations need higher energies to occur in the complexed acetonitrile, because of Cu(I) interaction with the lone pair of nitrogen, which rigidified the C−C≡N body. Indeed, this is also visible by the fact that the only vibrations, which show a smaller energy in the complex, are the one involving the CH_3 non-coordinated part of acetonitrile (ν_3 and ν_6, see Table 4). Another explanation for the acetonitrile small variation of peak can be the different states of both samples. In Cu(I) crystalline powder, the symmetry of the molecule as well as the symmetry of the crystal lattice need to be considered, because lattice vibrations could also influence the Raman spectrum.[11]

In Figure S1, $Cu(BF_4)_2$ spectrum contains the four vibrations modes of BF_4^- anion with energies of 765 (mode A_1), 355 (mode E), 525 and 1060 cm^{-1}.[12–14] Another vibration at 244 cm^{-1} correspond probably to a Cu-F vibration.[14] The same vibration is found at lower Raman shift 235 cm^{-1} for $[Cu(CH_3CN)_4]BF_4$ due the weaker interaction of Cu(I) with BF_4^-. Except the acetonitrile and BF_4^- peaks, $[Cu(CH_3CN)_4]BF_4$ Raman spectra has one specific signal coming from Cu(I) interaction with acetonitrile at 156 cm^{-1}. It is not surprising to find metal transition complexes with metal-ligand vibrations at low Raman shift.[15,16]

Table S1: Raman shifts for liquid acetonitrile and coordinated acetonitrile with Cu(I) in $[Cu(CH_3CN)_4]BF_4$.

			Raman shift / cm^{-1}		
Mode [6–9]	Class [6–9]	Assignment [6–9]	CH_3CN (liq.)	$[Cu(CH_3CN)_4]BF_4$	Δ / %
ν_8	E	C−C≡N bending	381	394	3.41
$2\nu_8$	A_1 + E		750	763	1.73
ν_4	A_1	C−C stretching	921	938	1.85

ν_7	E	CH_3 rocking	1043		
ν_3	A_1	CH_3 deformation	1376	1363	- 0.94
$\nu_7 + \nu_8$			1415		
ν_6	E	CH_3 deformation	1447	1369	- 5.39
$2\nu_4 + \nu_8$			2205		
ν_2	A_1	C≡N stretching	2251	2276	1.11
$\nu_3 + \nu_4$			2294	2306	0.52
$2\nu_3$	A_1		2735		
$\nu_3 + \nu_6$			2846		
$2\nu_6$			2882		
ν_1	A_1	Sym C−H stret.	2941	2944	0.10
ν_5	E	Asym C−H stret.	3004	3009	0.17

Viscosity of acetonitrile-propylene carbonate mixtures

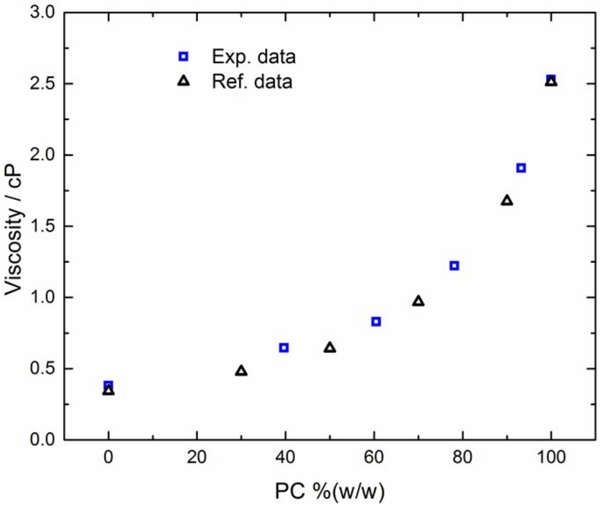

Supplementary Figure 2 Viscosity of the acetonitrile-propylene carbonate mixtures in function of the mass percentage of propylene carbonate in solution. The experimental data are following the same trend as the reported measurements in the publication of Moumouzias *et al.*[17]

Electrochemistry of copper

All potentials are expressed *vs.* the Cu wire in the solution of the given concentration of $[Cu(CH_3CN)_4]BF_4$. Hence, the potential of the Cu reference in equilibrium with 10mM Cu(I) solution in acetonitrile on the "non-aqueous standard copper electrode" scale (SCuE), *i.e. vs.* Cu(I) solution with the activity of 1 in equilibrium with Cu in acetonitrile is assumed to follow the Nernst equation considering the $\gamma Cu^+=1$, *i.e.* the potential of the reference is −0.118 V *vs.* SCuE in acetonitrile. To establish the relation with the ferrocene (Fc) scale recommended by IUPAC, the potential of the Fc^+/Fc couple *vs*. Cu/10mM Cu(I) in ACN was measured as 0.69 ± 0.01 V, *i.e.* the potential of the reference electrode used is −0.69 V *vs.* Fc^+/Fc.

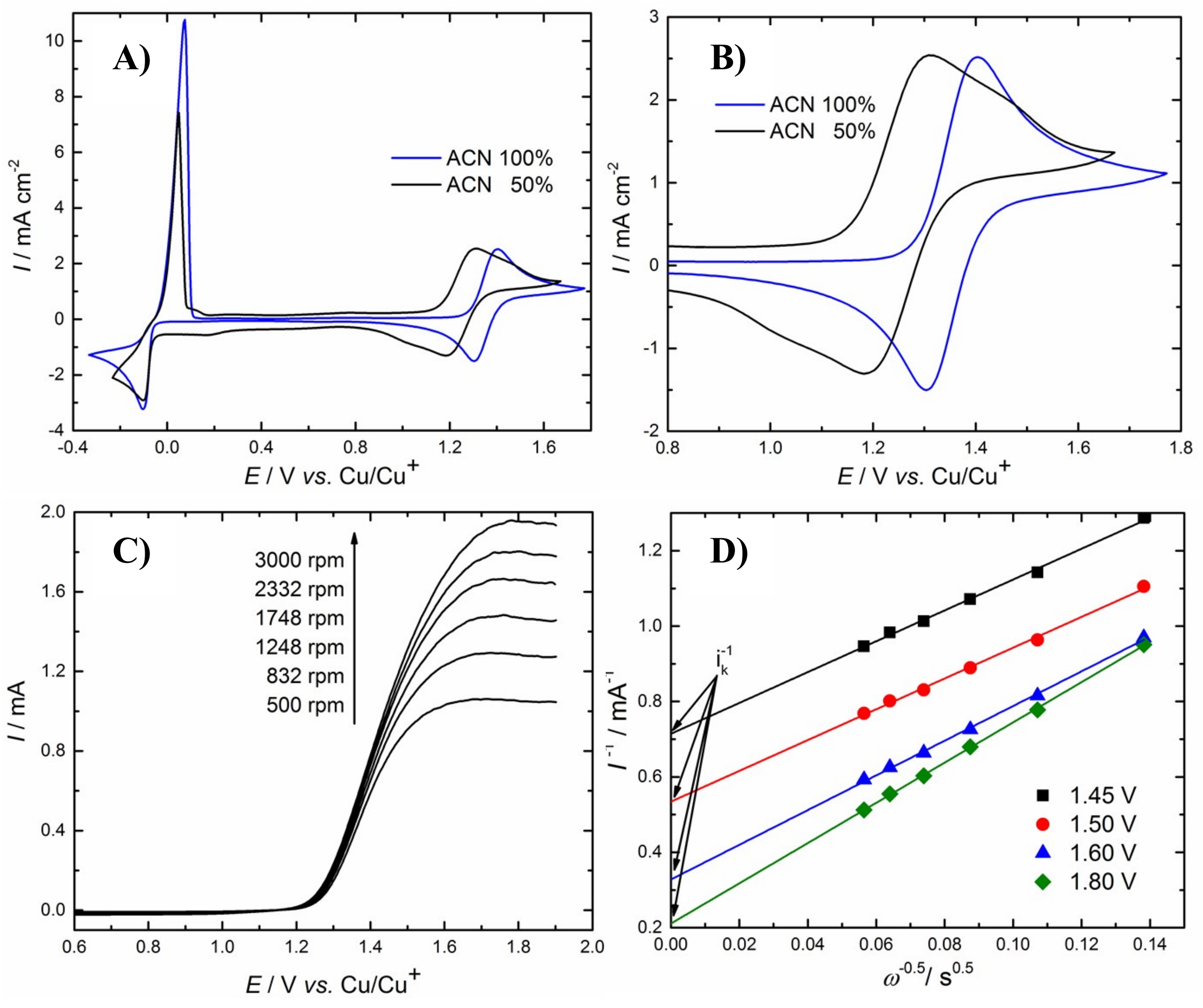

Supplementary Figure 3. Cyclic voltammetry and linear sweep voltammetry of $[Cu(CH_3CN)_4]BF_4$ (10 mM) in acetonitrile solutions (0.1 M $TEABF_4$) at 298.15 K. The scan rates are set at 100 $mV \cdot s^{-1}$.for the cyclic voltammetry and 10 $mV \cdot s^{-1}$ for the linear sweep voltammetry with the rotating disk electrode (RDE). CE = Pt wire, WE = Pt disk and RE = Cu/ Cu^+ A) Cyclic voltammetry showing the general electrochemical behavior of Cu^+ in acetonitrile and propylene carbonate. The deposition/stripping peak of the Cu^+/Cu has the specific shape, which is observed at 0.0 V (*vs*. Cu^+/Cu) with a high peak intensity for the stripping of the deposited Cu on the Pt WE. The peak after 1.0 V (*vs*. Cu^+/Cu) is showing a quasi-reversible redox couple for Cu^{2+}/Cu^+. B) The figure is focusing on the Cu^{2+}/Cu^+ couple and shows the effect of the solvent composition on the electrochemistry of Cu^{2+}/Cu^+. For 50%(*V*/*V*) of propylene carbonate in acetonitrile, the electron transfer occurs at 1.25 V (*vs*. Cu^+/Cu) and at 1.36 V (*vs*. Cu^+/Cu) for the pure acetonitrile electrolyte. Consequently, the potential expected for the RFB is lower when the propylene carbonate concentration is increasing. C) Linear sweep voltammetry from 500 to 3000 rpm with RDE for the Cu^{2+}/Cu^+ couple in pure acetonitrile solution. $E_{1/2}$ appears at 1.40 ± 0.01 V (*vs*. Cu/Cu^+) and shifts slightly to a higher value compared to the one from the cyclic voltammetry measurements. The relation described by Levich (Equation S1) between the limiting current (i_d) and the higher angular speeds (ω) allows the calculation of the diffusion coefficient, $D = 1.56 \pm 0.14 \cdot 10^{-5}$ cm² s⁻¹. D) With the Koutecký-Levich plot at E = 1.45, 1.5, 1.6 and 1.8 V (*vs*. Cu/Cu^+) calculated with the Equation S4, the kinetic current can be determined, as well as the heterogeneous rate constant (k^0) for the Cu^{2+}/Cu^+ couple in acetonitrile, $6.22 \pm 0.13 \cdot 10^{-3}$ cm s^{-1} (Equation S3). The value of the charge transfer coefficient (α) is calculated with the Equation S6 and has an experimental value of 0.25 ± 0.02. A significant difference for the diffusion coefficient of Cu(I) and kinetics of electron transfer for the Cu^{2+}/Cu^+ redox couple is observed between the acetonitrile solution and the 50%(*V*/*V*) of propylene carbonate in acetonitrile (respectively $D = 1.56 \cdot 10^{-5}$ cm^2 s^{-1}, $D = 1.16 \cdot 10^{-5}$ cm^2 s^{-1} and $k^0 = 6.22 \cdot 10^{-3}$ cm s^{-1}, $k^0 = 1.98 \cdot 10^{-3}$ cm s^{-1}). The decrease of the Cu(I) diffusion coefficient in solution containing propylene carbonate can be linked with the increase of viscosity in propylene carbonate solutions (Figure S2).

During linear sweep voltammetry at a rotating disk electrode, the equation S1, known as the Levich equation, describes the anodic limiting current (i_d):

$$i_d = 0.62nFAD_R^{2/3}\omega^{1/2}\nu^{-1/6}C_R^* \qquad (S7)$$

This current is totally limited by the mass-transfer, which depends on the viscosity ν, diffusion coefficient D_R and on the angular frequency of rotation ω. Consequently, D_R can be calculated from the evolution of the limiting current with ω.

For a general definition of a current response during a linear sweep voltammetry, the Koutecký-Levich equation combines i_d with the current i_K, which arises under purely kinetic controlled conditions:

$$i_K = FAk_f(E)C_R^* \qquad (S8)$$

$$k_f(E) = k^0 \exp\left[\alpha f\left(E - E^{0'}\right)\right] \qquad (S9)$$

$$\frac{1}{i} = \frac{1}{i_d} + \frac{1}{i_K} = \frac{1}{0.62nFAD_R^{2/3}\omega^{1/2}\nu^{-1/6}C_R^*} + \frac{1}{i_K} \qquad (S10)$$

By recording data at various angular speeds, it is possible to build Koutecký-Levich plots ($1/i$ *vs* $\omega^{-1/2}$), that can be used to extract i_K at the intercept and D_R from the slope. As the kinetic current is defined in the Butler-Volmer equation, the kinetic parameters can be calculated by using the Tafel behavior of the current for high overpotential.

$$i_K = i_0[e^{\alpha f\eta} - e^{-(1-\alpha)f\eta}] \qquad (S11)$$

$$i_K = i_0e^{\alpha f\eta} \qquad (S12)$$

Flow battery experiments

One redox battery is mounted with two half-cells of 3.4 mL (PermeGear Horizontal Cell from SES GmgH). The loading is done inside the glovebox to avoid the presence of oxygen and water. For the negative side (anode), a copper wire is used as an electrode and a platinum wire was used for the positive side (cathode). The area available for the ionic transport is 1.13 cm^2 with an opening diameter of 12 mm. Supplementary Figures 4a and 4b show 44 charge-discharge cycles measured with an H-cell in Fig. S5. Additional cycles are shown in Supplementary Fig. 6. At the beginning of the experiment, the device is fully discharged and both positive and negative electrolytes consist of 0.15 M $[Cu(CH_3CN)_4]BF_4$ (copper acetonitrile tetrafluoroborate) and 0.15 M $TEABF_4$ (tetraethylammonium tetrafluoroborate) as the supporting electrolyte. The first 40 charge/discharge periods were performed with a current density of 10 $mA\cdot cm^{-2}$ and the last four steps were done with a current density of 1 $mA\cdot cm^{-2}$.

As mentioned in the methods section, the potentials are corrected for the ohmic resistance induced by the membrane and electrolyte (Figure S4a). For the performance of the battery in Figure S4b, the efficiencies are calculated with all 44 cycles as detailed in the ESI (Eq. S1 and S2). The Coulombic and energy efficiencies are stable during 33 cycles after which they slightly decrease, and on average are around 95% and 51%. These efficiencies are comparable to other all Cu redox flow cells[18-20]. When lower current densities are applied, a better energy efficiency is obtained, as overpotential losses for the electrochemical reactions decrease. Indeed, an activation overpotential of approximately 50 mV is calculated at 10 $mA\cdot cm^{-2}$ *versus ca.* 10 mV at 1 $mA\cdot cm^{-2}$ at the onset of charge or discharge. These values can be determined from the potential drop when switching the current on, when *iR* correction is taken into account.

Charging and discharging at 10 $mA\cdot cm^{-2}$ allows the utilization of ca. 45 % of the total capacity, while a lower current density of 1 $mA\cdot cm^{-2}$ allows access to 84 % of the whole capacity during the cell charging. Relatively low current densities are employed to avoid high ohmic losses, as it is typical for systems employing non-aqueous electrolytes. By looking at the evolution of the Coulombic charge in Figure S4b, a loss of capacity is noticed. Almost 50% capacity loss is observed between the first and 40th charging step. Some of this capacity fade can be attributed to slow diffusion of oxygen and water into solution, leading to side reactions with oxygen. However, the major cause of the capacity fade is most likely the formation of dendrites on the Cu electrode upon charging, followed by detachment of the dendrites upon discharge. Some particles of Cu are then deposited at the bottom of the cell. This behaviour could be mitigated by common industrial copper plating additives.[21-24]

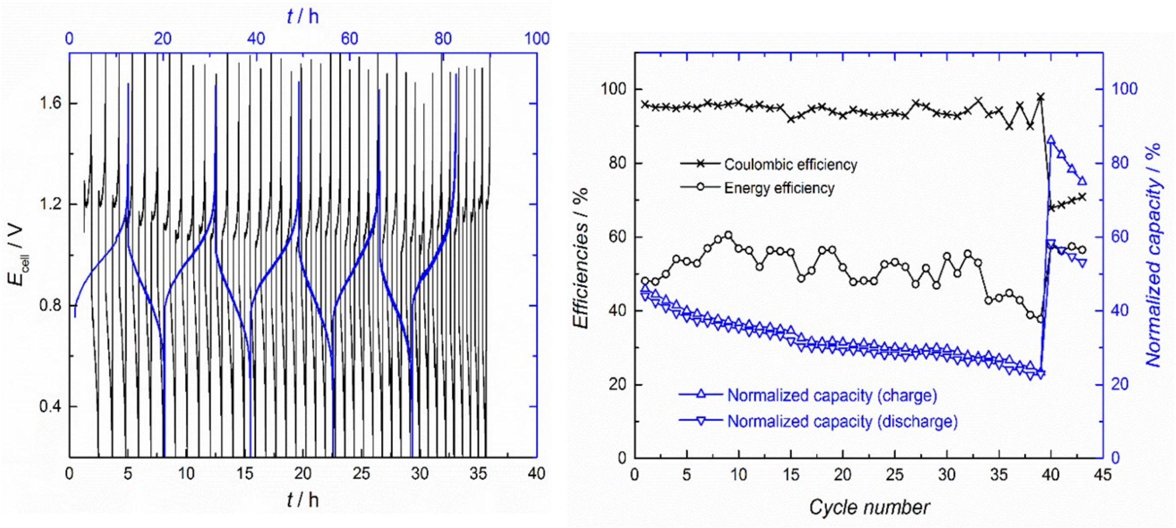

Supplementary Figure 4 Cu redox flow battery with $[Cu(CH_3CN)_4]BF_4$ (0.15 M) and $TEABF_4$ (0.15 M) and i = 10 and 1 mA cm^{-2}, respectively the black and blue curve, a) *iR* corrected potential cycling with time and b) efficiencies and normalized capacities of the battery for all cycles.

With the optimization of the cell, resistances between 0.5-3.0 Ω are reached with a typical flow cell. Considering the *iR* losses, the redox flow battery (RFB) is much more suitable than a miniaturized H-cell more than ten times higher resistance (10-25 Ω). The critical parameters are the distance between the electrodes, and the conductivities of the electrolyte and the membrane. The distance is much smaller and easier to control inside the RFB. Another important factor is the concentration of supporting electrolyte in acetonitrile and it can be increased by using more soluble species, like (lithium hexafluorophosphate) or LiTFSI (lithium bis(trifluoromethanesulfonyl)imide).

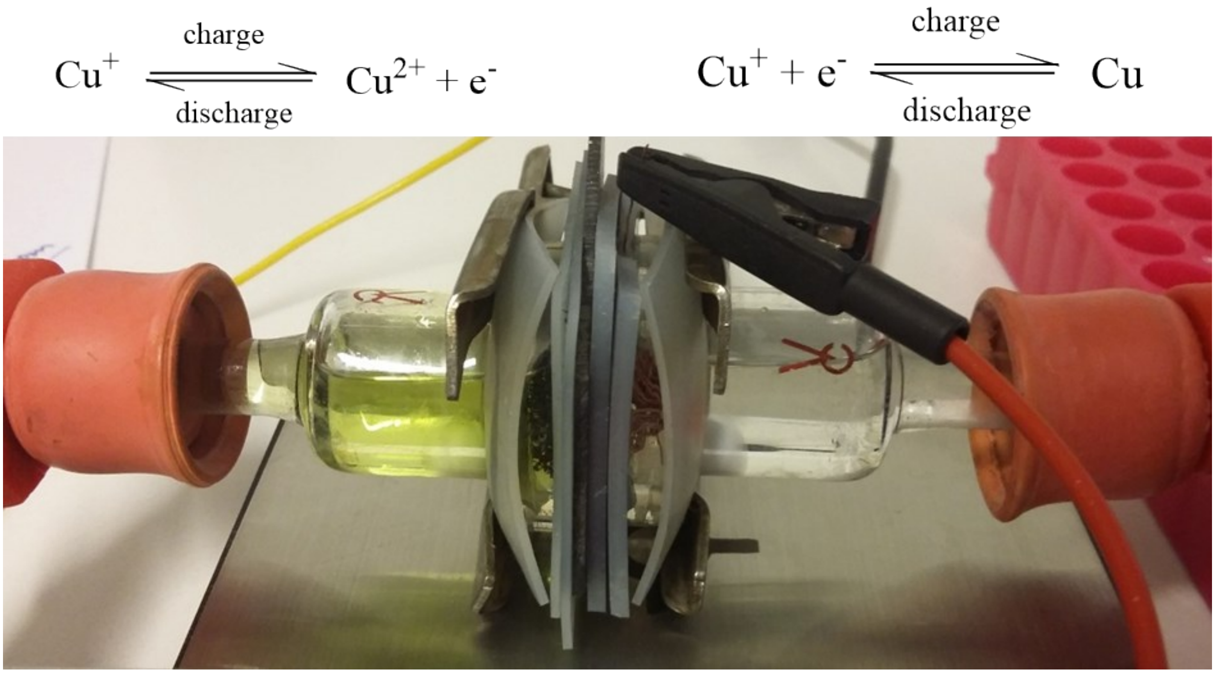

Supplementary Figure 5. Miniaturized H-cell with an anionic membrane, carbon (RVC) positive electrode and Cu negative electrode. One the left side, the positive electrolyte with the green color from the Cu^{2+} cation and on the right side, the negative electrolyte with the colorless solution from the Cu^{+}/Cu redox couple.

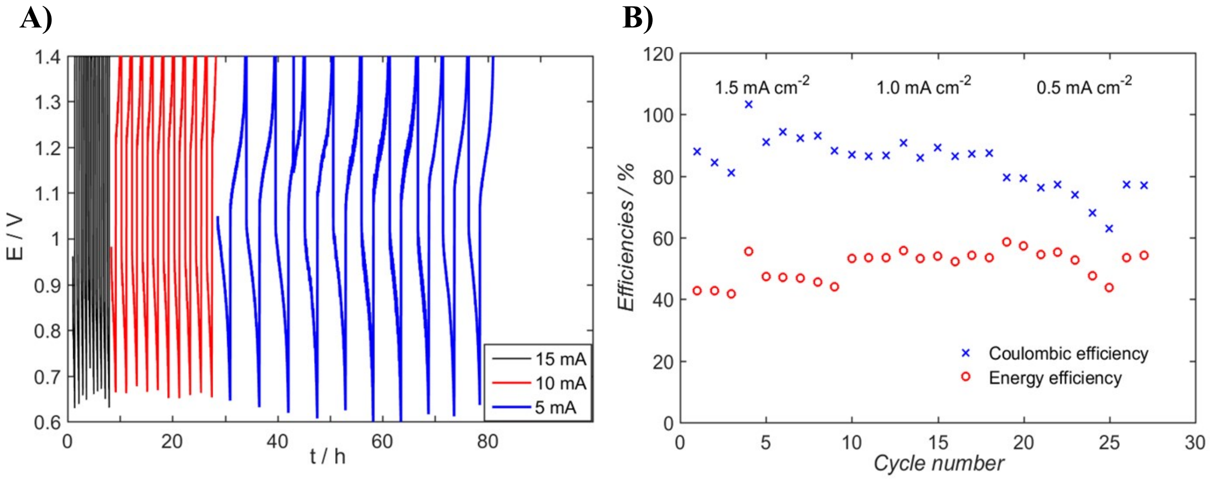

Supplementary Figure 6. H-cell experiment with charge/discharge cycling at 1.5, 1.0 and 0.5 mA cm^{-2}. The electrolyte is made with $[Cu(CH_3CN)_4]BF_4$ (0.15 mM) and 0.15 M ($TEABF_4$) in acetonitrile-propylene carbonate solvent (90%(*V*/*V*) of propylene carbonate). A) This graph shows the recorded voltage during the 10 cycles for the different current densities applied. B) The Coulombic efficiency is decreasing with time due to the loss of metallic Cu and probably water diffusion in the system which makes the oxidation of Cu^{+} to Cu^{2+} more irreversible. Regarding the energy efficiency between 40 and 60%, the current density plays an important role and with lower current, a lower difference of voltage is observed between the charging and discharging plateau.

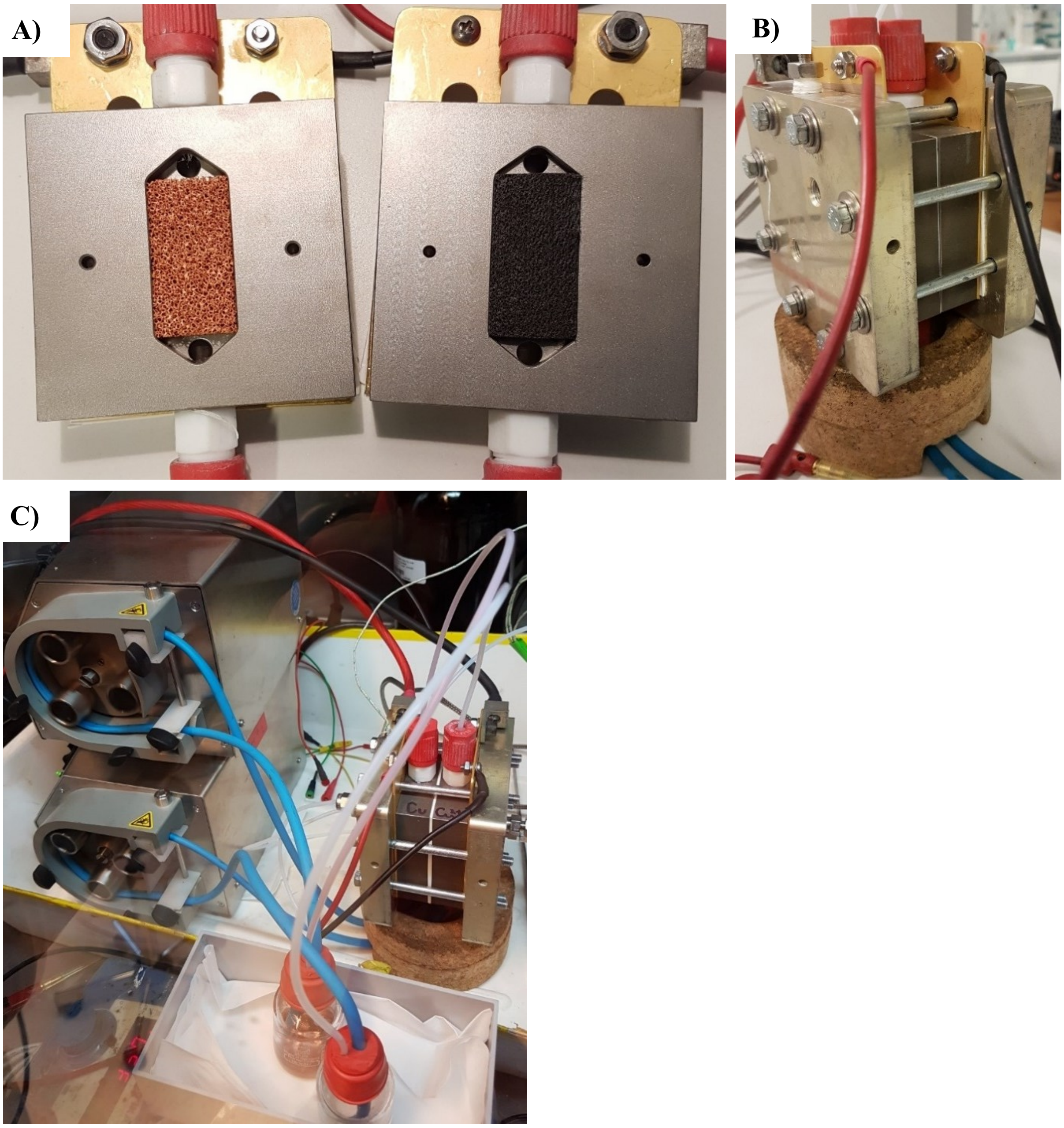

Supplementary Figure 7. A) The Ti negative current collector with metallic Cu foam electrode and the Ti positive current collector with the C-felt electrode have been designed especially for the testing of the Cu-RFB. Reticulated vitreous carbon foam was used instead of the Cu-foam for the slurry battery. B) The compressed electrochemical cell is used for the flow experiment with an anionic membrane between the two electrodes. C) The complete set-up includes peristaltic pumps for the flowing of the electrolyte, typical flow rate are between 40-45 mL min^{-1}. Tubing, O-ring and gaskets are made from polymers that can resist chemically to the organic solvent of the electrolyte like EPDM or expanded PTFE (Masterflex Solve-Flex from Cole-Parmer and 24SH-ePTFE gasket sheets from TEADIT).

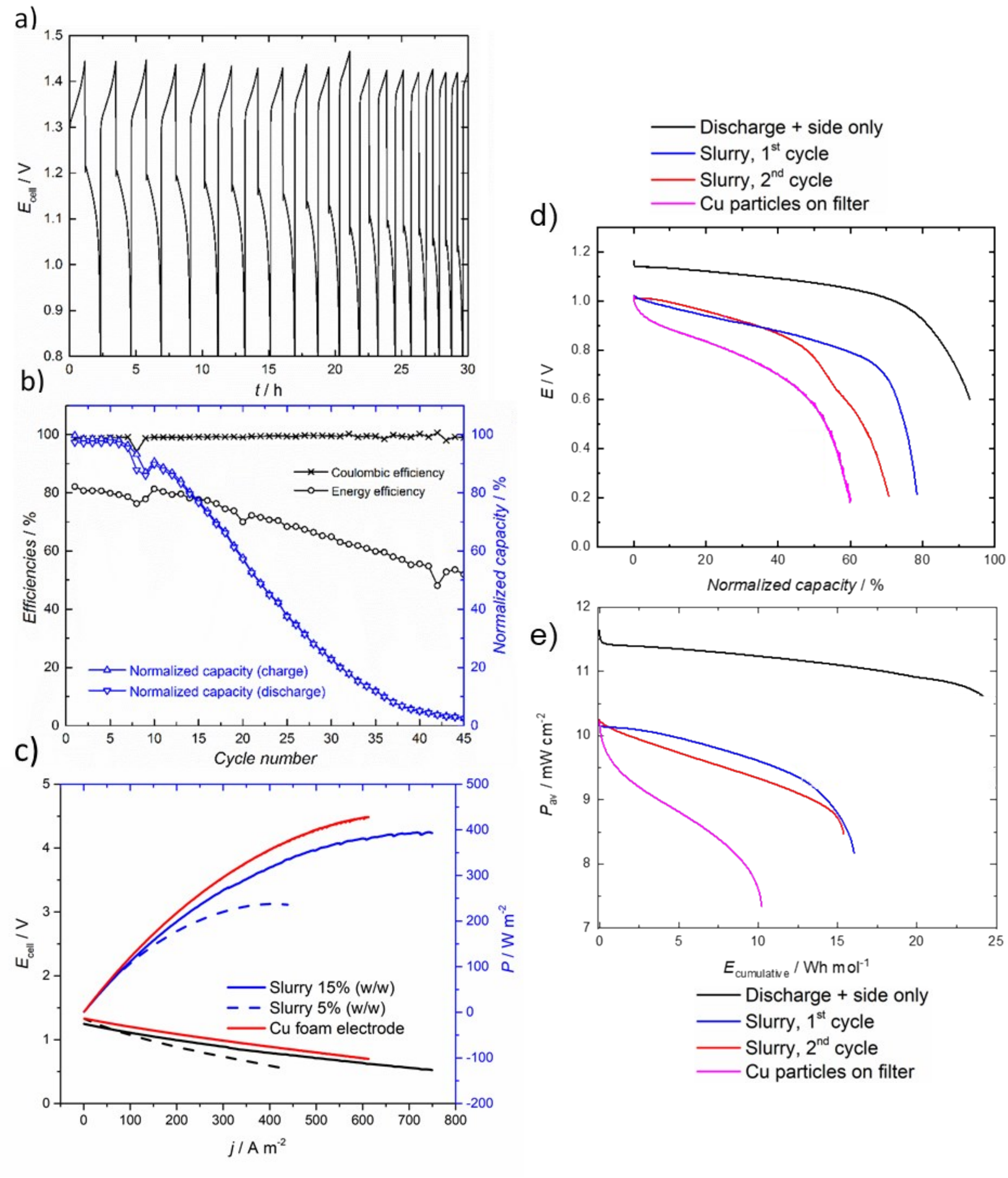

Supplementary Figure 8. *iR*-corrected data for the Cu redox flow battery with $[Cu(CH_3CN)_4]PF_6$ (0.15 M) and $LiPF_6$ (0.5 M) and i = 10 mA cm^{-2}, a) potential cycling (not *iR* corrected) with time and b) efficiencies and normalized capacities of the battery for all cycles. R increased gradually from 3 to 3.6 Ω (24 to 29 Ω cm^2). c) Power output with Cu foam and nanoslurry electrolytes with a composition of 50 vol% ACN containing 0.15 M $[Cu(CH_3CN)_4]BF_4$, at the flow rate of 40-45 mL min^{-1}. d) iR corrected discharge curves of the heat-regenerated RFB at 10 mA cm^{-2}. The positive electrolyte is composed of heat-regenerated $Cu(BF_4)_2$ (0.15 M) and $TEABF_4$ (0.15 M) in acetonitrile-propylene carbonate mixture and the negative electrolyte of $TEABF_4$ (0.15 M) in acetonitrile-propylene carbonate mixture. The acetonitrile is collected from the distilled fraction during the thermal disproportionation of the Cu(I). Additionally, on the negative side, the filter with the Cu particles is added in parallel to the membrane. R = 22.2, 12.1. 11.7 and 22.3 Ω cm^2 (or 2.78, 1.51, 1.46 and 2.79 Ω) for positive side only cell, Cu slurries and for Cu particles on filter. Volumes of the electrolytes on the positive side are 19, 10, 10 and 7 mL, respectively. **e)** Average power density output of the RFB during discharge *vs*. the cumulative energy output per mol of Cu^{2+}. Area of the membrane is 8 cm^2.

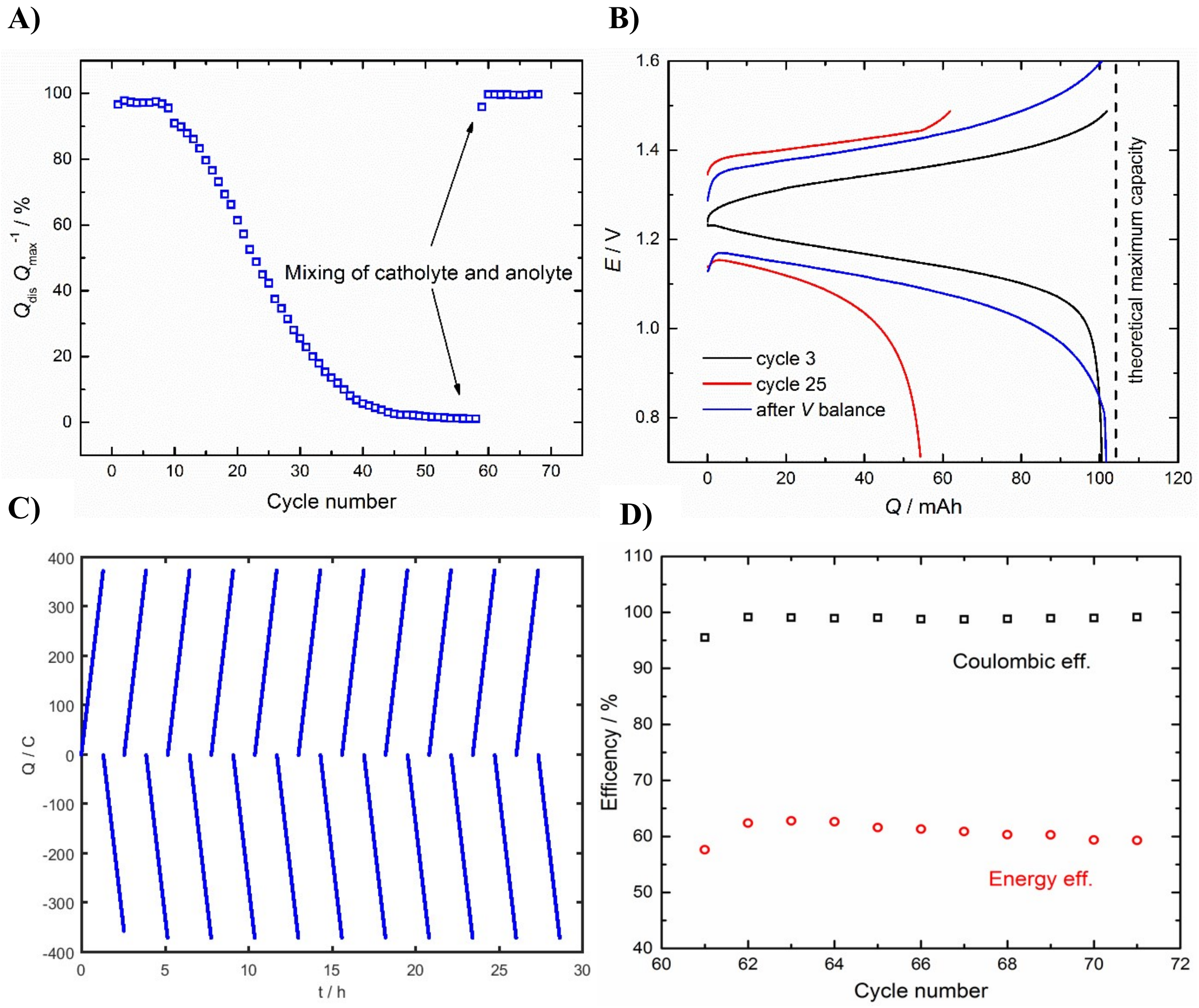

Supplementary Figure 9. Crossover phenomena between the positive and negative side during the cycling of the flow cell. The electrolyte solution is made with $[Cu(CH_3CN)_4]PF_6$ (0.15 M) and $LiPF_6$ (0.5 M). The applied current density is i = 10 mA cm^{-2}. C Evolution of the electrical capacity during the discharge. After 30 cycles, 20% of the maximum theoretical capacity is still discharged. After mixing of the totally discharge electrolyte containing mainly Cu^+ cation, the volume in both tanks is equilibrated and the full capacity is available again. B) The *iR*-corrected cycles 3, 25 and 61of the RFB experiment shows again the recovering of the capacity by mixing the electrolyte. Furthermore, the evolution of the voltage illustrates a modification of the internal resistance of the cell and explains the decreasing of energy efficiency with time. C) The capacity in C are plotted to observe the stability of the cycling after the 11 cycles following the volume balance. D) The energy efficiency is not totally recovered but is back to 60% after the volume balance.

Slurry synthesis

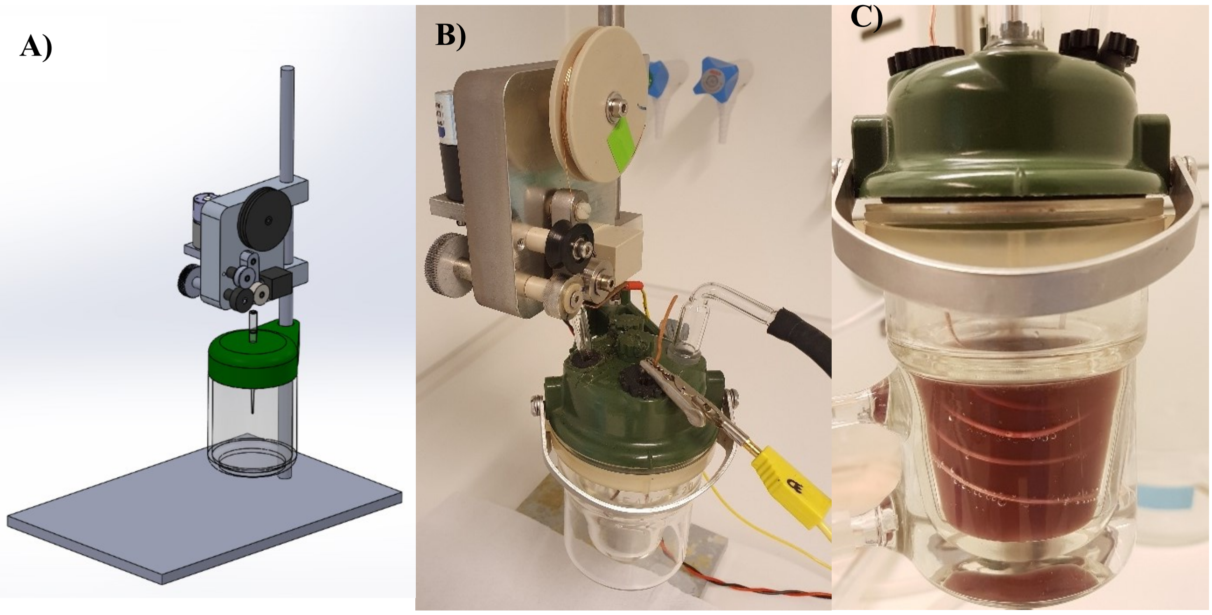

Supplementary Figure 10. A) Scheme of the motorized set-up for Cu NPs synthesis by corrosion method. B) Image of the same system. C) Image of the Cu NPs suspension in the bath for Cu corrosion (1M H_2SO_4 in water).

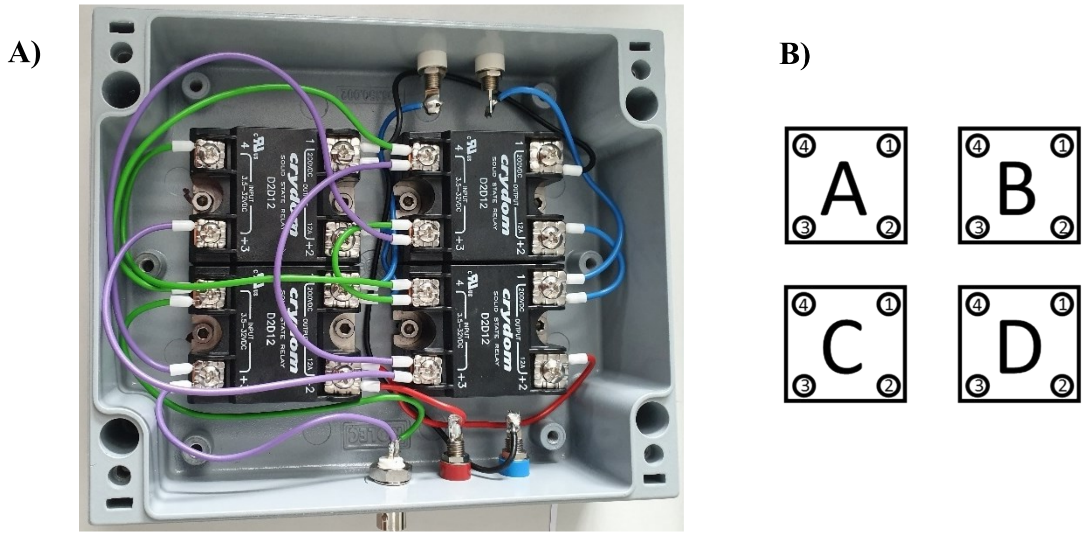

Supplementary Figure 11. A) Image of the 4 relays for the switch of polarization between the corroded wire and the counter electrode. B) Schematic representation of the 4 relays.

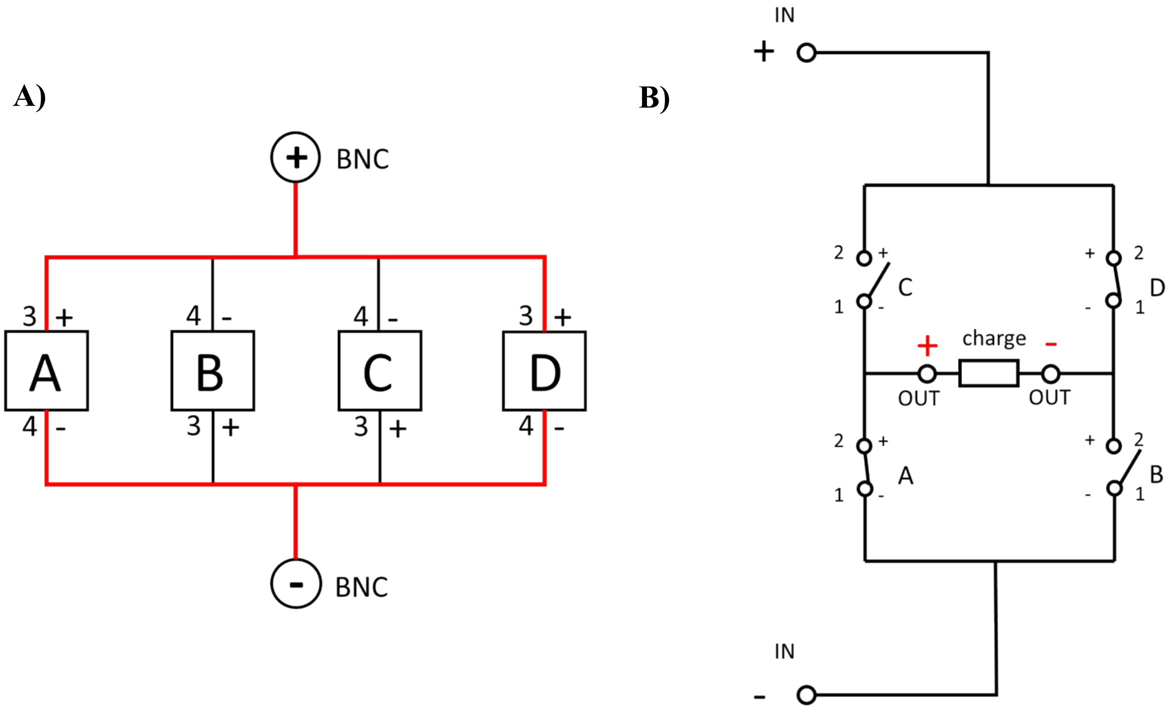

Supplementary Figure 12. A) Electrical scheme for the opening of the gates in the relays A and D. B) Electrical scheme for the output of the DC current with a square wave function.

The electronic circuit is the key part of the set-up and is briefly explained here The electronic system is composed of one power supply, one function generator for the tuning of the DC current and 4 relays (Supp. Fig. 11). The function generator module gives the frequency of the polarization modification at the Cu wire and the square wave shape for the DC current. The circuit presented in the Supp. Fig. 12 imitates an AC current with the utilization of a DC source. When the function generator activates the relay A and D (red path in Supp. Fig. 12a), the current from the power supply can cross these relays and the left output connection is negatively polarized and the right is positively polarized (red sign in Supp. Fig. 11b). In the opposite way, the activation of the relay C and B (black path in Supp. Fig. 12a) induces the other polarization at the Cu wires. This system produces the modification of the polarization at both Cu wire and with the high frequency for the Cu corrosion in the electrolyte.

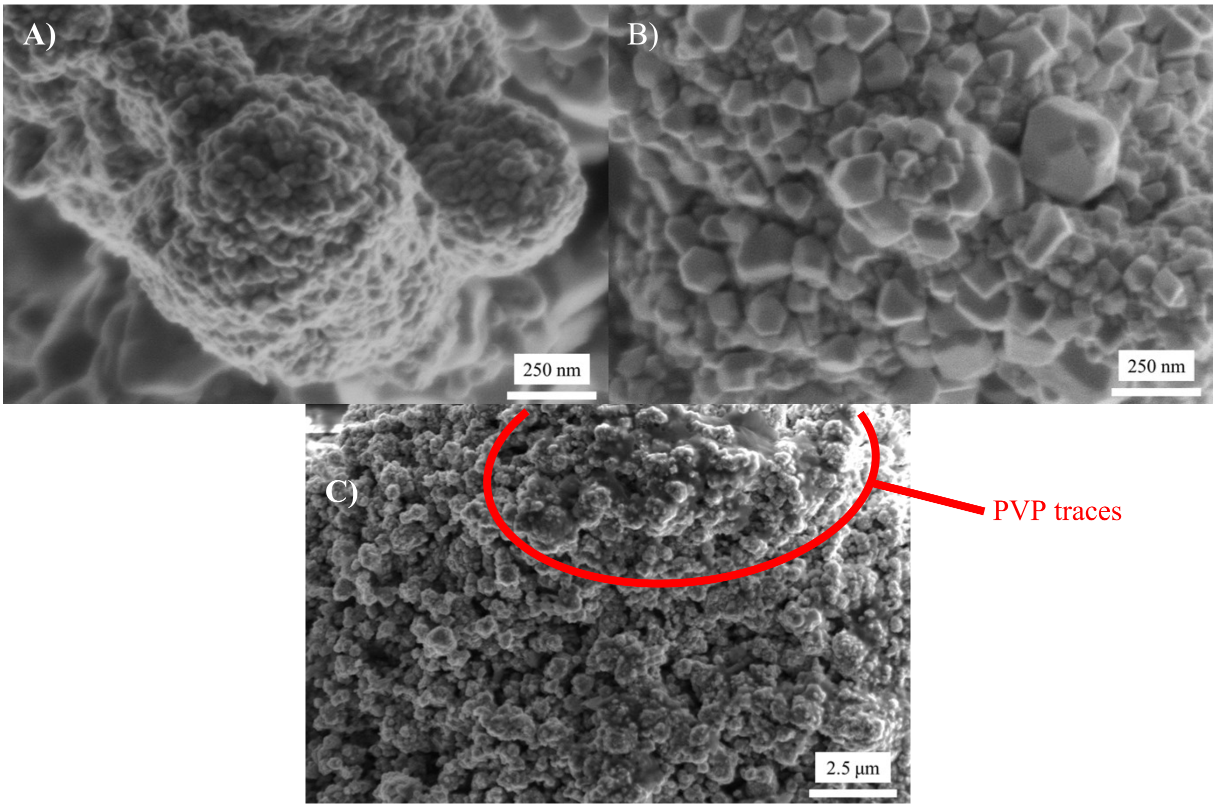

Supplementary Figure 13. SEM images of the Cu particles produced by the wire corrosion method. SE detection at 6.3 pA and 1.0 kV. Corrosion bath: 1M H_2SO_4 and 1 wt% PVP in water. A) Aggregation of Cu NPs (15-40 nm) in the final Cu particle. B) Cu NPs (50-250 nm). C) Image of the remaining PVP film on the Cu particles.

The solid Cu powder was imaged with SEM and a range of NPs going from 15-250 nm is detected in Supp. Fig. 13a-b. Comparing to M. Koper *and al*., the size of the NPs is larger than their average value of 5.2 nm.[25,26] The difference arises from the different choice of corrosion bath for the Cu NPs synthesis. Here the bath used is acidified with H_2SO_4 to protect the Cu particles from oxidation. In Supp. Fig. 12c, the remaining PVP stabilizer is not totally washed and some impurities of the polymer appears as a dark film in the upper part on the right side of the SEM image in Supp. Fig. 13c. Another important aspect of the NPs is highlighted with the SEM imaging; the agglomeration of the NPs is important during the cleaning process of the particles with particles sizes reaching 4-10 µm. The centrifugation of the NPs to remove water is obviously influencing the formation of larger particles with their accumulation at the bottom of the vial.

Thermal regeneration and differential scanning calorimeter measurements

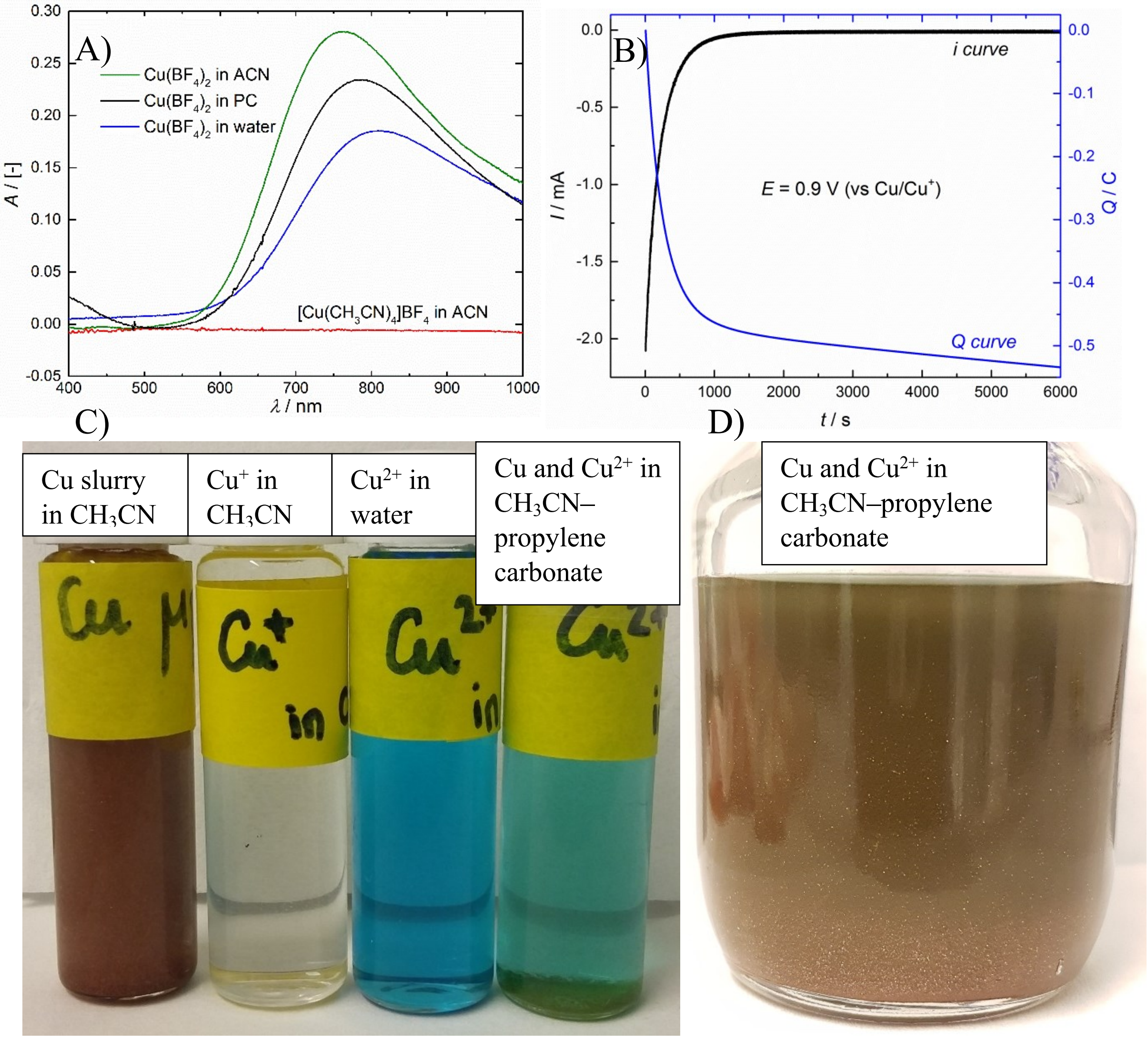

Supplementary Figure 14. Analysis of the thermal regeneration of the Cu^{2+}. A) UV-vis spectra for Cu^+ and Cu^{2+} in acetonitrile (ACN), Cu^{2+} in propylene carbonate (PC) is thermally produced (green curve). The conversion of Cu^+ during the disproportionation is observed by UV-vis spectroscopy of the final Cu^{2+} solution in propylene carbonate. The spectrum of $Cu(BF_4)_2$ in water shows the characteristic peak of Cu^{2+} with a maximum of absorbance around 810 nm.[27] In acetonitrile and propylene carbonate, this peak is shifted to smaller wavelength and appears around 760 and 785 nm. This confirms the Cu^{2+} presence in the final thermally generated solution. The comparison of the UV-vis spectra of Cu^+ and Cu^{2+} is easy and fast, because Cu^+ electronic configuration $[Ar]4s^0 3d^{10}$ cannot undergo absorption of light in the UV-vis range. Indeed, Cu^+ d orbital, which is completely full with 10 electrons, is not able to promote an electron with UV-vis light. In consequence, regardless the ligand and symmetry of the complex, no peak should be recorded for any Cu^+ solution. B) The electrolysis of the generated Cu^{2+} is promoted through its reduction at 0.9 V (vs. Cu/Cu^+) to quantify the amount of Cu^{2+} ions. From the initial concentration of Cu^+, the efficiency of the Cu^+ thermal disproportionation is determined around 98%. C) Cu^{2+} cation looks blue in water or green/turquoise in acetonitrile-propylene carbonate mixtures due to the absence of water. As expected in the case of a pure Cu^+, no trace of Cu^{2+} appears and the solution is transparent. D) Cu-Cu^{2+} solution after thermal treatment of a $[Cu(CH_3CN)_4]BF_4$ (0.15 mM) and $TEABF_4$ (0.3 M) in acetonitrile-propylene carbonate solvent (90%(V/V) of propylene carbonate). Shiny Cu particles are visible in the Cu^{2+} electrolyte.

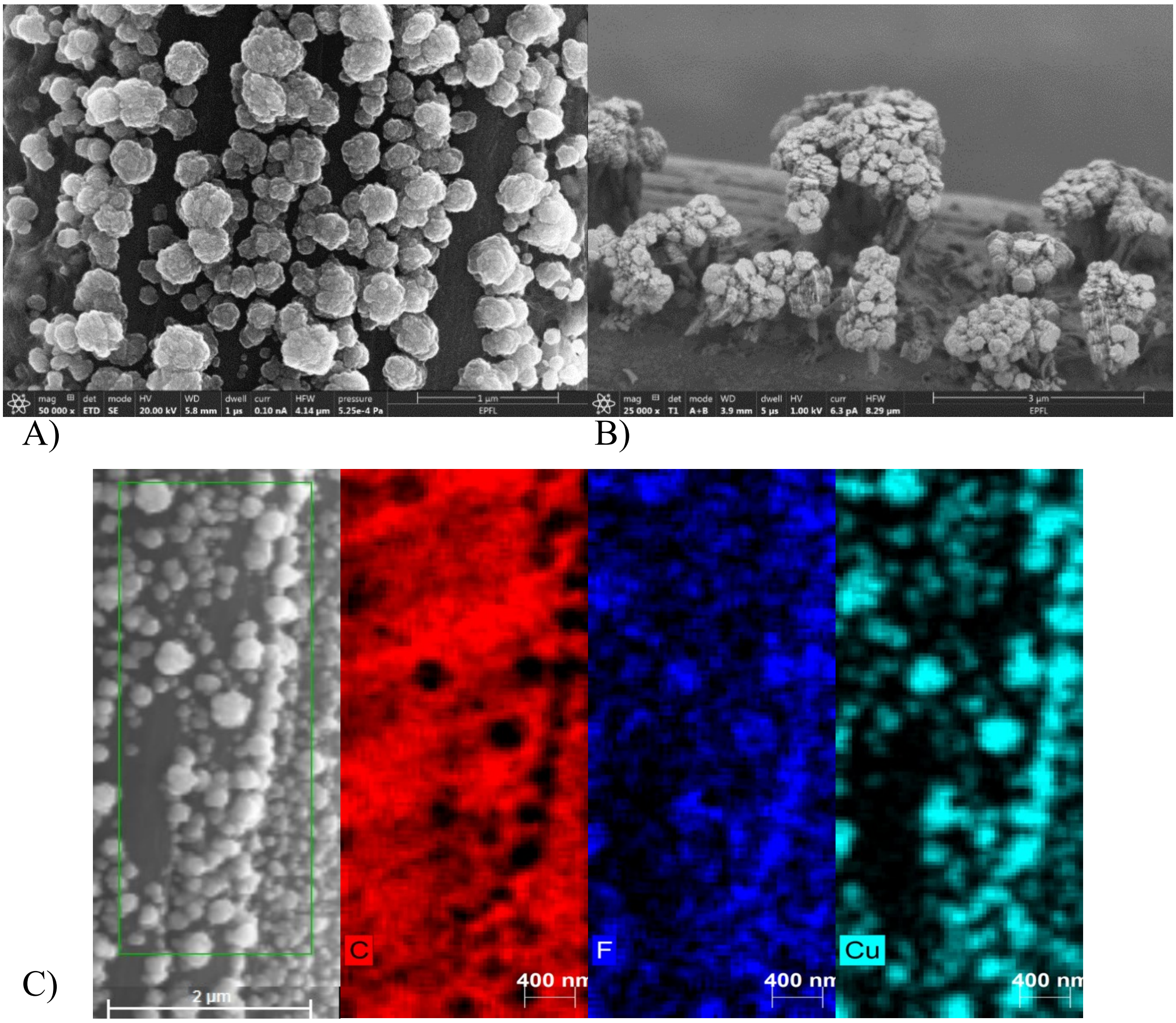

Supplementary Figure 15. SEM images of thermally regenerated Cu on carbon fibre with electron beam at A) 20 kV and B) 1 kV, C) EDX scans of regenerated Cu on carbon fibre.

In the SEM images, which are shown in Figure S15a, the secondary electron (SE) detection is achieved and Cu particles can be observed on the surface of the carbon fibres. Their shape looks more or less spherical. Also, some edge effects appear with brighter contours of some Cu clusters. This means that more SE can escape from the side of the particles and this confirms that Cu clusters are not simply recovering the carbon fibre like a flat homogenous layer. To improve the topographical contrast and to have a better idea of the shape of the regenerated Cu, the electron accelerating voltage has been decreased to 1 kV and the detection is done in-lens (Fig. S15b). With a lower voltage, the volume of interaction inside the sample will be smaller and less backscattered electron (BSE) will reach the detector. Consequently, in Figure S15b, there is less contrast between the carbon fibre and Cu, which appears brighter at high voltage with more BSE. However, by analysing carefully the topology, the thermal regeneration seems to form spherical Cu clusters made of nanoparticles and gives a shape similar to a cauliflower when it is nucleated on carbon fibre. In addition to the electron microscopy imaging, chemical characterisation is carried out in Figure S15c. The goal of this is to confirm the presence of the Cu and also to check if some other chemicals appear in the sample. With a silicon drift detector, energy dispersive X-ray (EDX) mapping has been recorded at 15 keV. Carbon coming from the support is observed in red and the particles containing Cu in light blue. Beside of that, the EDX analysis revealed fluorine in the sample. This can be explained by the composition of the solution, that is heated for the thermal regeneration, and contains BF_4^- counter anion of $[Cu(CH_3CN)_4]^+$. It is not surprising to detect fluorine.

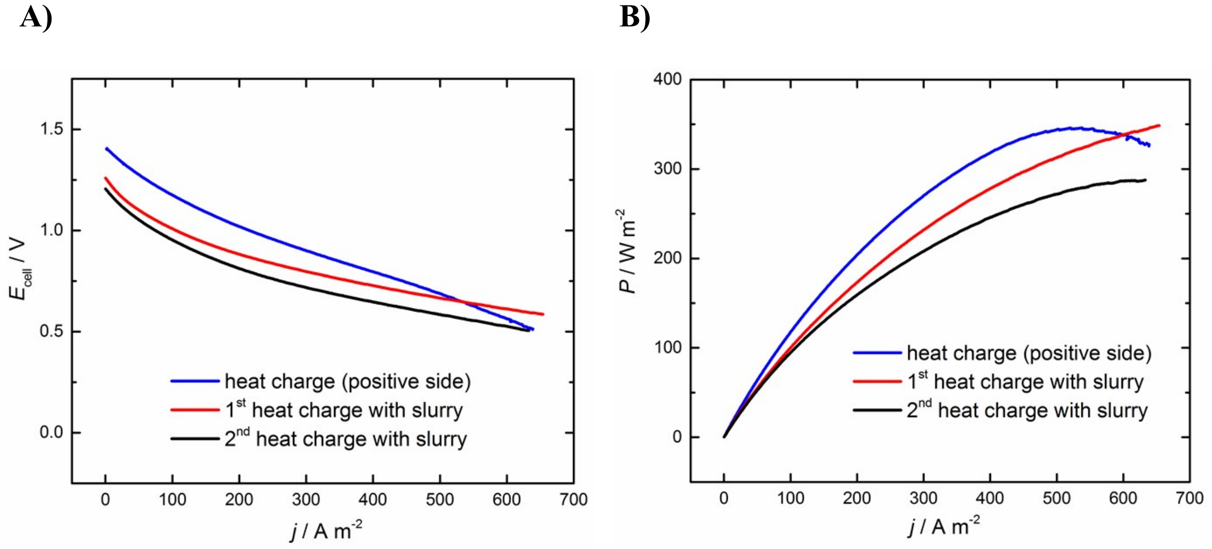

Supplementary Figure 16. A) Polarization curves (with iR correction, R = 0.9-3 Ω) and B) corresponding power production of the Cu-RFB after heat regeneration. The starting solution for the thermal treatment of Cu(I) (0.3 M) to Cu-Cu(II) has a solvent composition of 50% acetonitrile in propylene carbonate. The polarization curves is done inside the cell with Cu foam electrode, named heat charge positive side (blue curve), inside a cell with the charged Cu slurry electrode showing the first discharge (red curve) and second discharge (black curve) after two consecutive heat charge processes. With the compensation of the cell resistance, the expected power production increases compared to the experimental data. This indicates that if the conductivity of the RFB can be improved, the final power production would be more efficient.

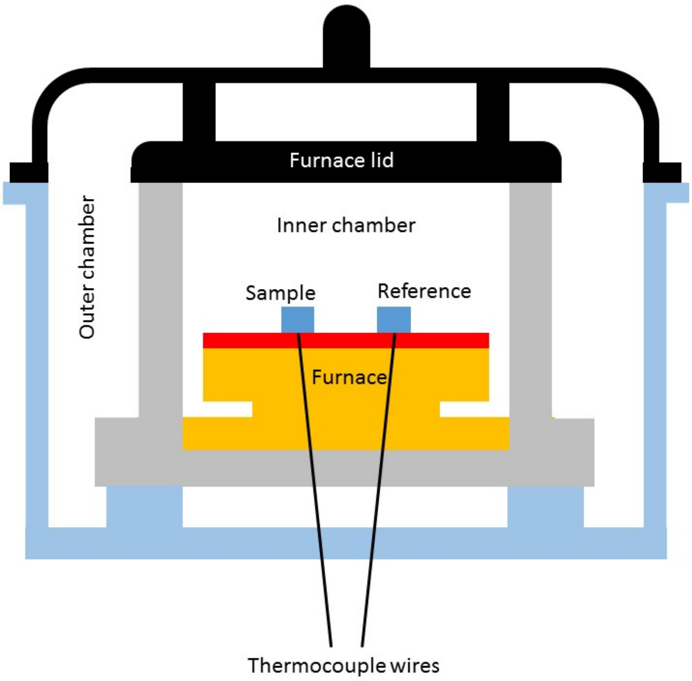

Supplementary Figure 17. Illustration of the DSC furnace

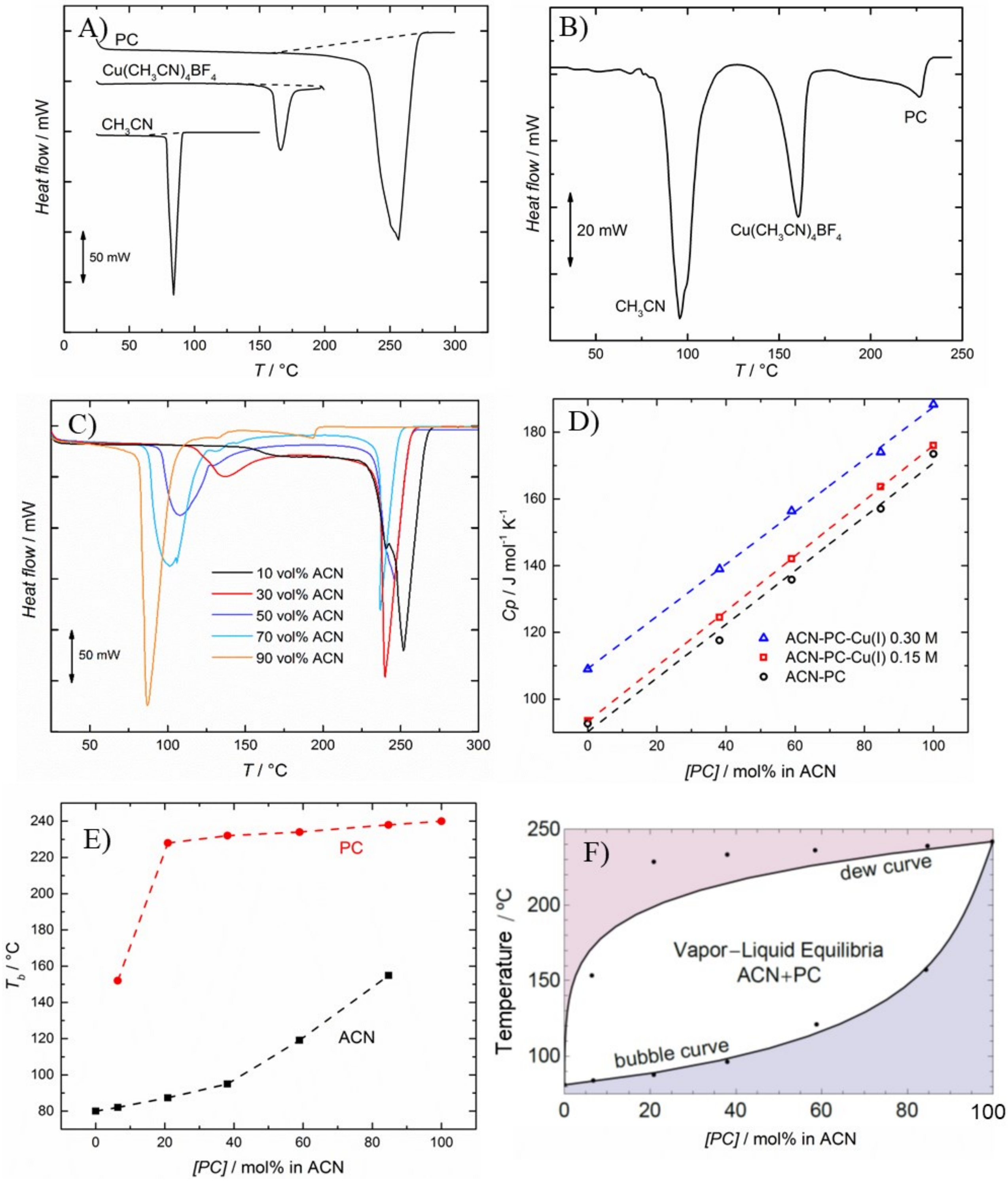

Supplementary Figure 18. a) DSC of acetonitrile at 5 K min^{-1}, propylene carbonate and solid [Cu(CH$_3$CN)$_4$]BF$_4$ at 20 K min^{-1}, b) DSC for acetonitrile-propylene carbonate mixture of saturated [Cu(CH$_3$CN)$_4$]BF$_4$ at 20 K min^{-1} with 90 vol% acetonitrile. c) DSCs of acetonitrile-propylene carbonate mixture with 10 to 90 vol% acetonitrile, d) *C*p evolution of acetonitrile-propylene carbonate mixtures containing [Cu(CH$_3$CN)$_4$]BF$_4$ according to the propylene carbonate content. e) Temperatures of the vaporization of acetonitrile and propylene carbonate in the acetonitrile-propylene carbonate mixtures, measured at 20 K min^{-1}. f) Estimated vapour-liquid equilibrium curves for ACN+PC system.

Table S2. Enthalpies and temperatures of vaporization/decomposition for acetonitrile, propylene carbonate and $[Cu(CH_3CN)_4]BF_4$ from DSC.

Molecule	This work		Literature	
	ΔH / kJ·mol^{-1}	T / °C	ΔH / kJ·mol^{-1}	T / °C
acetonitrile	32.4 ± 1.6	81 ± 1	29.8-34.8 [a]	81-82 [b]
propylene carbonate	54.0 ± 1.8	242 ± 2	50.9-56.3 [c]	241-242 [d]
$Cu(CH_3CN)_4BF_4$	106.8 ± 4.4	161 ± 1	-	159-161 [e]

a[28,29] b[28,30] c[31-32] d[28,33] e[34]

The efficiency of the heat-to-power conversion can be estimated based on the thermodynamic data, as shown in equation S13. The factor 2 in the nominator is required because the electrolytes from both sides of the battery need to be regenerated. Here, only evaporation of acetonitrile is considered, although some extra energy will be required to also evaporate some PC, as shown by the vapour-liquid equilibrium curves in Fig. S18f.

$$\eta = \frac{W_{elec}}{2Q_{tot}} = \frac{nFE_{cell}c_{[Cu(I)(ACN)_4]^+}}{2(Q_{sol} + Q_{vap} + Q_{rxn})} = \frac{nFE_{cell}c_{[Cu(I)(ACN)_4]^+}}{2(\Delta T * C_p * c_{tot} + \Delta H_{vap}^{ACN} * c_{ACN} + \Delta H_{rxn}^{Cu(I)} * c)}$$

Table S3 shows the contribution of each term considering 0.3 M $[Cu(CH_3CN)_4]BF_4$ solution in different solvents, considering a temperature difference from 70 to 160 °C.

Table S3. Calculation of the heat to power conversion according to Eq. S13 for a solution of $[Cu(CH_3CN)_4]BF_4$ (0.3 M).

	acetonitrile 10%(V/V)	acetonitrile 30%(V/V)	acetonitrile 50%(V/V)	acetonitrile 70%(V/V)	acetonitrile 100%(V/V)
E_{cell} / V	1.05	1.15	1.25	1.30	1.36
W_{clec} / kJ L^{-1}	30.4	33.3	36.2	37.6	39.4
Q_{rxn}(Cu(I)) / kJ L^{-1}	32.0	32.0	32.0	32.0	32.0
$Q_{vap}(CH_3CN)$ / kJ L^{-1}	62.1	186.3	310.6	434.8	621.1
Q_{sol} / kJ L^{-1}	201	202	198	194	191

$\eta_{\text{ther. regen.}}$ / %	5.1	4.0	3.3	2.8	2.3

The electrical output that can be extracted for the heat-regenerated electrolyte is higher for solution with higher acetonitrile content because of the wider electrochemical window of Cu^+ (Fig. S3). Regarding the energy input, which is needed to drive the thermal disproportionation of the Cu^+, the heat of vaporization for acetonitrile, as well as the heat required to heat the solution to 160 °C are thetwo most important factors. Heat required for vaporization of acetonitrile increases significantly for high acetonitrile containing solutions. Consequently, the energy conversion efficiency is better for solutions with low acetonitrile content even if the final cell voltage is smaller. 5.1% theoretical efficiency could be improved for example by increasing the concentration of copper electrolyte to 1.5 M, as shown in the calculations in Table S4. The apparent molar heat capacity of the electrolyte estimated from the data shown in Fig. S18D was used to estimate $Q_{\text{sol.}}$ More accurate estimations would require measurements of the heat capacity of 1.5 M copper solutions. This system would be able to obtain a theoretical efficiency of 13 %. The efficiencies for different temperature ranges (from low temperature to 160 °C) are shown in Supplementary Fig. 19.

Table S4. Estimation of the heat to power conversion according to Eq. S13 for a solution of $[Cu(CH_3CN)_4]BF_4$ (1.5 M).

	acetonitrile 10%(V/V)	acetonitrile 30%(V/V)	acetonitrile 50%(V/V)	acetonitrile 70%(V/V)	acetonitrile 100%(V/V)
E_{cell} / V	1.05	1.15	1.25	1.30	1.36
W_{clec} / kJ L^{-1}	152	166	181	188	197
Q_{rxn}(Cu(I)) / kJ L^{-1}	160	160	160	160	160
$Q_{\text{vap}}(CH_3CN)$ / kJ L^{-1}	62.1	186	311	435	621
Q_{sol} / kJ L^{-1}	349	403	454	457	514
$\eta_{\text{ther. regen.}}$ / %	13.3	11.1	9.8	8.9	7.6

The heat for the disproportionation ($Q_{rxn}(Cu^+)$) is approximated to be equal for all the solvent mixtures because the same concentration of Cu^+ is considered (0.3M).

For the heat capacities (Cp) of the different solutions, which is used to calculated the heat needed to warm the solution, the trend is to heat more for high propylene carbonate content to reach a given temperature (Fig. S18 d). This can be explain by the propylene carbonate thermal properties, which has to receive more thermal energy than acetonitrile to be heated. This behaviour explains why the energy to warm the solution is more important for the propylene carbonate rich ones. However, another effect not considered here but also influencing the Q_{sol} value, is the fact that the temperature of vaporization of acetonitrile is changing within the different mixtures with propylene carbonate. Acetonitrile is thermally stabilized in the liquid state by the presence of propylene carbonate. This trend can be observed in Fig. S18 c and e. This effect on acetonitrile vaporization leads to an increase of thermal energy for the heating of the solution before the acetonitrile vaporization and Cu^+ disproportionation occur. To improve this efficiency, the energy required for heating up the solution should be minimized. One option would be to replace propylene carbonate with a co-solvent with lower heat capacity.

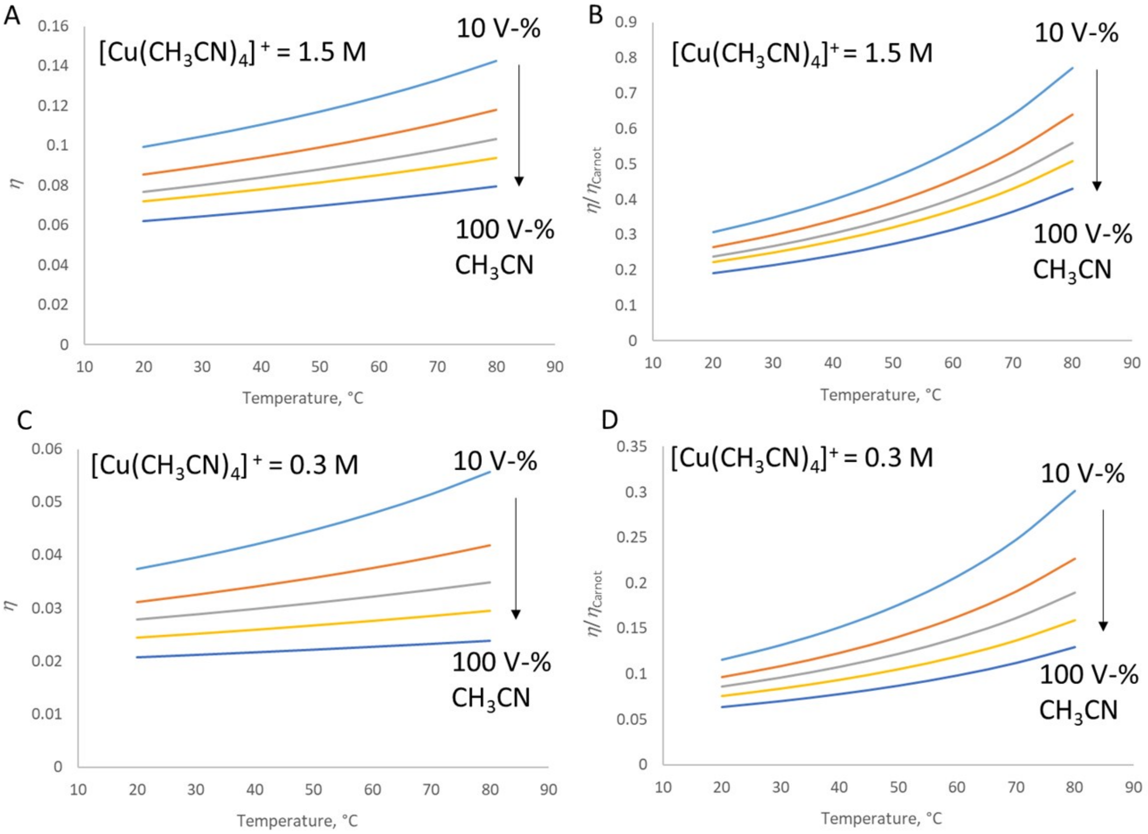

Supplementary Figure 19. Dependence of the efficiency versus the lower temperature for different volume ratios of CH_3CN and PC, considering 1.5 M and 0.3 M Cu(I) salts. Efficiencies are shown on the left, while efficiencies in relation to the Carnot cycle efficiency are shown on the right.

Supplementary references

1. Hathaway, B. J., Holah, D. G. & Underhill, A. E. 468. The preparation and properties of some bivalent transition-metal tetrafluoroborate–methyl cyanide complexes. *J. Chem. Soc. Resumed* 2444–2448 (1962). doi:10.1039/JR9620002444
2. Kubas, G. J., Monzyk, B. & Crumbliss, A. L. Tetrakis(Acetonitrile)Copper(I) Hexafluorophosphate. in *Inorganic Syntheses* (ed. Shriver, D. F.) 90–92 (John Wiley & Sons, Inc., 1979).
3. Persson, I., Penner-Hahn, J. E. & Hodgson, K. O. An EXAFS spectroscopic study of solvates of copper(I) and copper(II) in acetonitrile, dimethyl sulfoxide, pyridine, and tetrahydrothiophene solutions and a large-angle x-ray scattering study of the copper(II) acetonitrile solvate in solution. *Inorg. Chem.* 32, 2497–2501 (1993).
4. Walton, P. H. *Beginning Group Theory for Chemistry*. (OUP Oxford, 1998).
5. Sathyanarayana, D. N. *Vibrational Spectroscopy: Theory and Applications*. (New Age International, 2015).
6. Neelakantan, P. Raman spectrum of acetonitrile. *Proc. Indian Acad. Sci. - Sect. A* 60, 422–424 (1964).
7. Evans, J. C. & Bernstein, H. J. Intensity in the Raman effect: IV. Raman intensity sum rules and frequency assignments for CH_3CN, CD_3CN, CH_3CCl_3, and CD_3CCl_3. *Can. J. Chem.* 33, 1746–1755 (1955).
8. Sadlej, J. Interpretation of the i.r. and Raman spectrum of acetonitrile solutions of electrolytes in the CN stretching region. *Spectrochim. Acta Part Mol. Spectrosc.* 35, 681–684 (1979).
9. Shimanouchi, T. Tables of Molecular Vibrational Frequencies Consolidated Volume I. 1–160 (1972).
10. Dimitrova, Y. Vibrational frequencies and infrared intensities of acetonitrile coordinated with metal cations: an ab initio study. *J. Mol. Struct. THEOCHEM* 343, 25–30 (1995).
11. Sasic, S. *Pharmaceutical Applications of Raman Spectroscopy*. (John Wiley & Sons, 2008).
12. Lozinšek, M. *et al.* Syntheses, crystal structures and Raman spectra of $Ba(BF_{4)}(PF_6)$, $Ba(BF_4)(AsF_6)$ and $Ba_2(BF_4)_2(AsF_6)(H_3F_4)$; the first examples of metal salts containing simultaneously tetrahedral BF_4^- and octahedral AF_6^- anions. *J. Solid State Chem.* 182, 2897–2903 (2009).
13. Sequeira, C. & Santos, D. *Polymer Electrolytes: Fundamentals and Applications*. (Elsevier, 2010).
14. Addison, C. C. *Inorganic Chemistry of the Main-Group Elements*. (Royal Society of Chemistry, 1976).

15. Suffren, Y., Rollet, F.-G. & Reber, C.Raman spectroscopy of transition metal complexes: molecular vibrational frequencies, phase transitions, isomers, and electronic structure. *Comments Inorg. Chem.* 32, 246–276 (2011).
16. Pavel, I. *et al.* Vibrational behavior of transition metal cupferronato complexes. Raman and SERS studies on nickel(II) cupferronato complexes. *Vib. Spectrosc.* 23, 71–76 (2000).
17. Moumouzias, G., Panopoulos, D. K. & Ritzoulis, G. Excess properties of the binary liquid system propylene carbonate + acetonitrile. *J. Chem. Eng. Data* 36, 20–23 (1991).
18. Peljo, P., Lloyd, D., Doan, N., Majaneva, M. & Kontturi, K. Towards a thermally regenerative all-copper redox flow battery. *Phys. Chem. Chem. Phys.* **16**, 2831–2835 (2014).
19. Kratochvil, B. & Betty, K. R. A Secondary Battery Based on the Copper(II)-(I) and (I)-(0) Couples in Acetonitrile. *J. Electrochem. Soc.* **121**, 851–854 (1974).
20. Leung, P., Palma, J., Garcia-Quismondo, E., Sanz, L., Mohamed, M.R. & Anderson, M. Evaluation of electrode materials for all-copper hybrid flow batteries. *J. Power Sources* **310**, 1–11 (2016).
21. Crousier, J. & Bimaghra, I. Electrodeposition of copper from sulphate and chloride solutions. *Electrochim. Acta* **34**, 1205–1211 (1989).
22. Plieth, W. Additives in the electrocrystallization process. *Electrochim. Acta* **37**, 2115–2121 (1992).
23. Healy, J. P., Pletcher, D. & Goodenough, M. The chemistry of the additives in an acid copper electroplating bath: Part II. The instability 4,5-dithiaoctane-1,8-disulphonic acid in the bath on open circuit. *J. Electroanal. Chem.* **338**, 167–177 (1992).
24. Jovic, V. D. & Jovic, B. M. Copper electrodeposition from a copper acid baths in the presence of PEG and NaCl. *J. Serbian Chem. Soc.* **66**, 935–952 (2001).
25. Yanson, A.I., Rodriguez, P., Garcia-Araez, N., Mom, R.V., Tichelaar, F.D. & Koper, M.T.M. Cathodic Corrosion: A Quick, Clean, and Versatile Method for the Synthesis of Metallic Nanoparticles. *Angewandte Chem. Int. Ed.* **50**, 6346–6350 (2011).
26. Feng, J., Chen, D., Sediq, A.S., Romeijn, S., Tichelaar, F.D., Jiskoot, W., Yang, J. & Koper, M.T.M. Cathodic Corrosion of a Bulk Wire to Nonaggregated Functional Nanocrystals and Nanoalloys. *ACS Appl. Mater. Interfaces* **10**, 9532–9540 (2018).
27 Dodi, G., Hritcu, D., Lisa, G. & Popa, M. I. Core–shell magnetic chitosan particles functionalized by grafting: Synthesis and characterization. *Chem. Eng. J.* 203, 130–141 (2012).
28. Haynes, W. M. *CRC Handbook of Chemistry and Physics, 95th Edition*. (CRC Press, 2014).
29. Vladimír Majer & Vaclav Svoboda. *Enthalpies of vaporization of organic compounds: a critical review and data compilation*. (Blackwell Scientific Publications, 1985).
30. Di Cave, S. & Mazzarotta, B. Isobaric vapor-liquid equilibria for the binary systems formed by acetonitrile and aromatic hydrocarbons. *J. Chem. Eng. Data* 36, 293–297 (1991).

31. Hong, C. S., Wakslak, R., Finston, H. & Fried, V. Some thermodynamic properties of systems containing propylene carbonate and ethylene carbonate. *J. Chem. Eng. Data* 27, 146–148 (1982).
32. Stephenson, R. M. & Malanowski, S. Properties of Organic Compounds. in *Handbook of the Thermodynamics of Organic Compounds* 1–471 (Springer Netherlands, 1987). doi:10.1007/978-94-009-3173-2_1
33. Rajapakse, N., Finston, H. L. & Fried, V. Liquid-liquid phase equilibria in the propylene carbonate+ methyl isobutyl ketone+ water system. *J. Chem. Eng. Data* 31, 408–410 (1986).
34. Hathaway, B. J., Holah, D. G. & Postlethwaite, J. D. 630. The preparation and properties of some tetrakis(methylcyanide)copper(I) complexes. *J. Chem. Soc. Resumed* 3215–3218 (1961).